**Proceedings of the ASME 2018 International Mechanical Engineering Congress and Exposition**
**IMECE2018**
**November 9-15, 2018, Pittsburgh, USA**

# IMECE2018-86937

# PULSATORY MIXING OF LAMINAR FLOW USING BUBBLE-DRIVEN MICRO-PUMPS

Brandon Hayes[1,2], Austin Hayes[3], Matthew Rolleston[2], Alexander Ferreira[3], and James Krisher[3]

[1]Department of Biomedical Engineering, Rochester Institute of Technology
[2]Department of Microelectronics and Electrical Engineering, Rochester Institute of Technology
[3]Department of Mechanical Engineering, Rochester Institute of Technology

## ABSTRACT

Microfluidics differ from conventional fluid flows in that viscous forces dominate. As a result, microfluidics offer unprecedented control over fluid flows. The precise manipulation of fluids can be applied anywhere from healthcare in medical diagnostics to pharmaceutical companies miniaturizing reactions to reduce reagent consumption. In order to apply microfluidics as a comprehensive solution, unit operations must be performed – such as mixing, sorting, dilution, and much more. This work investigates mixing using thermal inkjet technology. Unlike macroscopic fluid flows with turbulence, transport phenomena become restricted in microfluidics. Active mixing approaches apply external forces (such as thermal or electric) to enhance mixing. This work focuses on a utilizing thermal inkjet technology as an active mixing technique. Y-shaped microfluidic channels have been built utilizing CNC and laser cutting manufacturing techniques. Fluid is delivered to each port via external syringe pumps. Each Y-shaped channel contains thermal inkjet (TIJ) resistors built using conventional microfabrication techniques. The resistors vaporize water and generate drive bubbles that act as active micro-mixers. The extent of mixing was characterized and studied in order to access the feasibility of TIJ resistors as integrated, compact micro-mixers in microfluidics.

## 1 INTRODUCTION

Microfluidics holds the potential to revolutionize the chemical and biomedical spaces [1]. Lab-on-a-chip technologies present the ability to shift from a laboratory test center with instrumentation specific for each medical test to hundreds of tests miniaturized on a single silicon die [2]. However, fluid handling at the micro-scale presents entirely different problems than that at the macro-scale. Upon reaching millimeter and micrometer channel dimensions, fluid flow is dominated by viscous forces. As such, fluid flow becomes laminar. Laminar flow can be thought of as discrete laminae moving in a fluid. While dyes and chemicals may mix somewhat via natural diffusion, larger ($\mu m$ size) particles will not mix in such a system. Consider a lab-on-a-chip technology containing both cells and reagents, such a system must be able to perform a unit mixing operation.

In general, microfluidic mixing approaches are divided into two categories: passive and active mixing [3]. In a passive approach, the channel geometry or roughness is used to mix the fluid without addition of external energy. Passive mixing is characterized by large mixing lengths. Stroock et al. implemented a herringbone geometry on the base of a microfluidic channel to create local disruption to the fluid flow [4]. However, a large mixing length of 500 mm was required for uniform mixing. Liu et al. demonstrates the influence of a square wave mixer, a three-dimensional serpentine mixer and a staggered herringbone mixer [5]. Again, a large length scale is required where they found a length to diameter ratio of 13 for the herringbone mixer was needed. In order to further reduce the length scale required, active mixing is used. Owen et al. [6] created a rotating magnetic microbead mixer capable of full mixing within 270 $\mu m$ of length. As such, in order to miniaturize lab-on-a-chip devices, the mixing length must be minimized.

Govyadinov, Torniainen, Kornilovitch, and Markel illustrate an active mixing technique utilizing HP inkjet technology [7]. Inkjet technology consists of a thermal inkjet (TIJ) resistor that is designed to boil a thin layer of fluid to create a bubble that acts as an electro-mechanical transducer [8]. That is, an electrical pulse is converted to a mechanical bubble capable of moving and mixing fluid [9]. The dynamics of bubble formation are complex. The expansion and collapse of this bubble occurs within 50 $\mu$s [10]. It is useful to consider the boiling process first in

equilibrium before considering its transient behavior. Figure 1 defines the boiling process in its equilibrium state. First, single phase convection occurs as the liquid temperature approaches the saturation temperature. After this point, nucleate boiling occurs where cavities on the surface cause a bubble to nucleate. With rising heat flux, nucleate boiling occurs more chaotically and vapor is formed at increasing rates on the surface. At a certain point, termed critical heat flux (CHF), this vapor blankets the surface and acts as an insulating film. In a transient system, the surrounding liquid remains sub-cooled. That is, the bulk fluid does not heat up substantially. As such, sub-cooled boiling occurs where the heated surface causes local nucleation and bubble growth at the surface. However, due to the cooler surrounding liquid, bubbles quickly collapse in the fluid. This explosive bubble expansion and collapse holds promise for microfluidic mixing. Furthermore, this boiling regime is termed metastable boiling and falls off the equilibrium boiling curve as shown in figure 1.

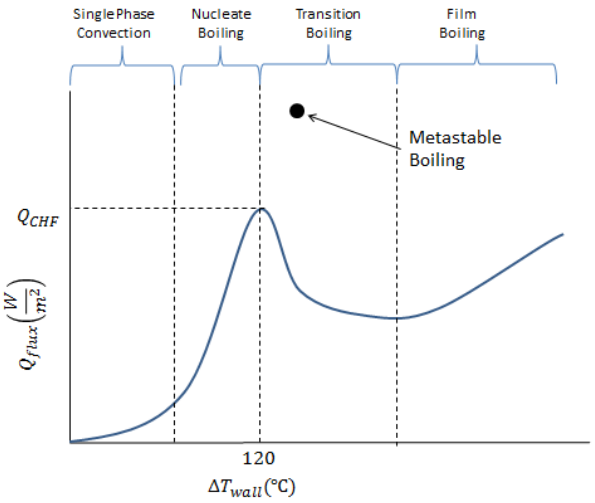


**FIGURE 1**: Boiling Curve Showing Metastable Boiling

In this study, we experimentally demonstrate the ability to extend TIJ technology to mix laminar flow. Furthermore, we demonstrate the ability of TIJ resistors to behave as micro-mixers at both nucleate and metastable boiling regimes. By utilizing TIJ resistors, our mixing length has the potential to be scalable. That is, the mixing length scale is dependent on the size of the TIJ resistor. As fluid passes over the resistor, it mixes on each firing pulse. Therefore, this type of pulsatory active mixing technique has the potential to continuously mix fluid as it passes over top of the resistor surface within a microchannel. Thus, the mixing length becomes the length of the resistor. We analyzed resistors on the order of 200-300 $\mu$m. However, microfabrication techniques make it possible to fabricate resistors significantly smaller than these dimensions.

## 2 Design and Fabrication

### 2.1 Mechanical Setup

A mechanical design was made to house a silicon wafer, create a fluidic seal, define the microfluidic channels, and deliver fluid. At the base, a plexiglass fixture holds a silicon wafer. This fixture also provides structural support to apply pressure in order to seal the system. Next, the diced silicon wafer (25 mm x 33 mm) was placed on top of the plexiglass fixture. A silicon gasket was laser cut to define the microchannel geometry and this gasket is placed on top of the wafer. Next, a manifold is machined out of plexiglass which holds the inlet and outlet ports to attach to a syringe pump. A top aluminum spacer was fastened to the assembly with set screws to apply pressure to seal the device. Figure 2a depicts an exploded view of the mechanical design. The inlet ports are attached to the side of the assembly in order to facilitate electrical connections to the wafer.

### 2.2 Resistor Microfabrication

Using a surface microelectromechanical system (MEMS) process, micro-heaters were fabricated on silicon substrates. Figure 3 describes the fabrication process. Primarily, 5 $\mu m$ of $SiO_2$ was deposited via tetraethyl orthosilicate (TEOS) chemical vapor deposition. This will act as a thermally resistant buffer layer between the silicon substrate and the micro-heater device (figure 3a). A 1 $\mu m$ thick layer of polysilicon was then deposited via low pressure chemical vapor deposition (figure 3b). The polysilicon was then subsequently doped with a dose of $2 \times 10^{16}$ $cm^{-3}$ of $P^{31}$ at 70 keV by ion implantation and annealed at 1050 $°C$. The targeted sheet resistance of the doped polysilicon was 20 $\Omega$/sq (figure 3c). Level 1 lithography was done to define the polysilicon. Device dimensions were targeted to have a length of 300 $\mu m$ and width of 200 $\mu m$ (figure 3d). To make contact to the polysilicon, 1 $\mu m$ of aluminum was DC sputtered (figure 3e). Level 2 lithography was done to define the aluminum (Figure 3f). In order to electrically insulate the device from the surrounding fluid, approximately 70 nm of $SiO_2$ was deposited (figure 3g). $SiO_2$ over the contact pads was then etched in a buffered oxide etch to enable electrical contact (figure 3h).

## 3 Experiment

### 3.1 Fluid Delivery and Optical Setup

A syringe pump (Harvard Apparatus 55-4143) was equipped with two syringes and used as the mechanism for controlling fluid flow in the device. Figure 2b depicts the tube connection system. Prior to testing, the syringes were loaded from a purge

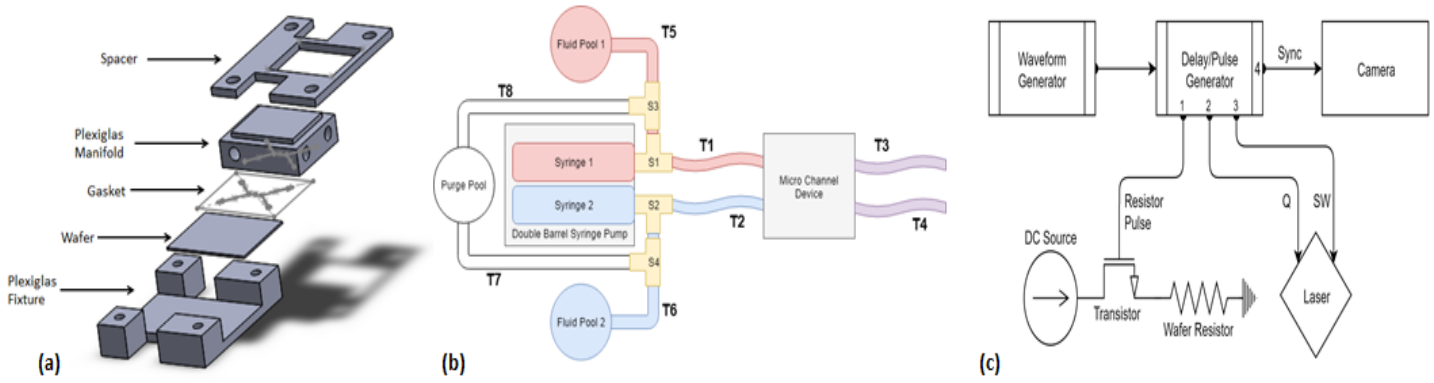


**FIGURE 2**: Mechanical and Optical Subsystems – detailed overview of mechanical and optical setups utilized in this study. (a) expanded CAD model of mechanical fixture, (b) fluid delivery setup, and (c) stroboscopic optical setup.

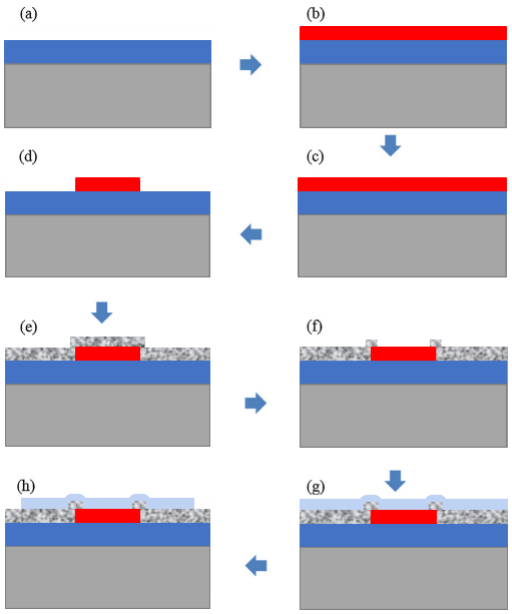


**FIGURE 3**: Micro-heater Process Flow. Color code: silicon (gray), silicon dioxide (blue), polysilicon (red), aluminum (marble), and thin silicon dioxide layer (light blue).

pool of DI water and flushed through the system in order to wet all surfaces and eject air bubbles. Four stopcocks allow the new syringe charges to be withdrawn while keeping the system closed to the atmosphere. All tubing was 1/16" ID Tygon in 2 ft lengths and all connections are standard luer-lock fittings. A standard microscope with a 10X objective lens was utilized to visualize the silicon wafer through the viewport illustrated in figure 2a.

### 3.2 Drive Bubble Stroboscopic Setup

To visualize drive bubble formation (and more generally the boiling mode), a transient event of approximately 50 $\mu s$ must be observed. Due to the repeatable nature of this expansion and collapse process on the resistor's surface, stages of bubble formation and collapse can be imaged through the use of a strobed light source – we utilized a 532 nm laser (New Wave SOLO I 15Hz). The firing of the laser was synchronized to a firing pulse sent to the resistor. The camera's exposure began the instant the laser was fired. As such, by incrementally adjusting the delay between resistor pulse and laser firing, different points in the bubble's lifespan were imaged.

A waveform generator (Agilent 33220A) provided the governing frequency of the system, set at 15 Hz, while a pulse generator (BNC Berkeley Nucleonics 500) triggered both the resistor and camera. The delay between Q, (charge-up signal) and SW (switch signal), determines the power of the laser and subsequent brightness of the image, here on the order of 120 $\mu s$. The delay between SW and the resistor pulse was initially set to zero and then incremented by 1 $\mu s$ to step through the entire formation and collapse of the bubble. The event was imaged using a IDT X3MP-U-4 camera which is synchronized to the SW pulse of the laser.

### 3.3 Particle Tracking and Post-Processing

Videos were processed using a MATLAB implementation of the IDL Particle Tracking algorithms [11]. Figure 4 illustrates the progression of the tracking processes at each step. Lagrangian particle tracking of 7 $\mu$m particles was performed as illustrated in figure 4a. Particle identification in MATLAB is illustrated in figure 4b and figure 4c depicts the particle streamlines colored in accordance to its average velocity (using a jet color scheme). After tracking, data was exported to .mat files for further processing and analysis. In order to maintain accuracy, particle displacements must be significantly less than that of the average particle

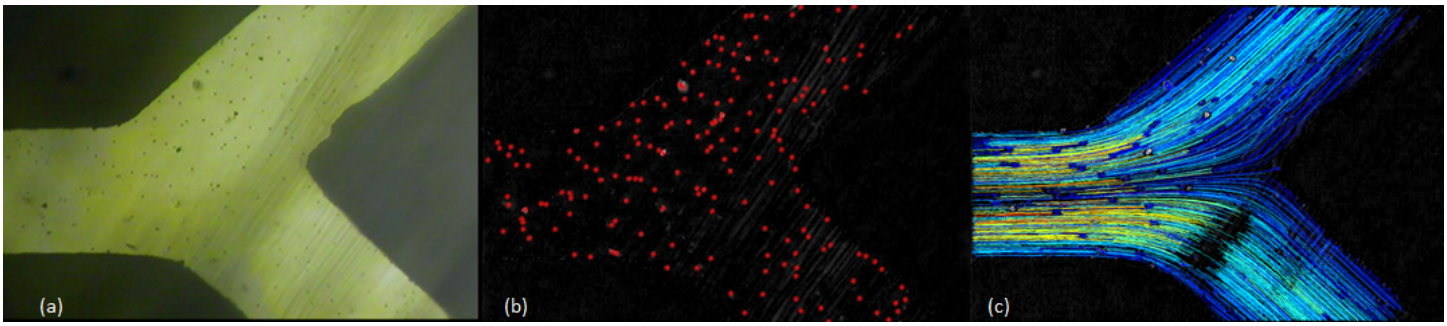


**FIGURE 4**: Particle Tracking Process Overview – (a) initial frame with 7 $\mu$m particles, (b) MATLAB processing of initial frame to identify particles, and (c) MATLAB processing of particle tracks to generate particle streamlines colored in accordance to a jet colormap quantified by average velocity.

separation. However, a sufficient number of particles must be tracked to probe the flow field. As such, this necessitates long video file recordings.

## 4 Mixing Characteristics

### 4.1 Macroscopic Mixing

Unlike microfluidic flows with chemical species, the diffusion of 7 $\mu$m particles follows the Stokes-Einstein relationship with diffusion coefficients on the order of $10^{-14}$ $m^2/s$ which is 10,000 times smaller than that of fluorescein (representative of most chemical species). Therefore, particles enable clear visualization of flow lamina. Since particles follow the flow field in a microfluidic channel, it is important to understand the rectangular flow profile. Simplification of Navier-Stokes equation for incompressible, steady-state flow yields equation 1 with boundary conditions highlighted below. Solution to this PDE yields the rectangular flow profile described by figure 5.

$$\frac{\partial^2 V_x}{\partial y^2} + \frac{\partial^2 V_x}{\partial z^2} = -\frac{\Delta P}{\mu L} \tag{1}$$

$$V_x(0,z) = 0 \tag{2}$$
$$V_x(a,z) = 0 \tag{3}$$
$$V_x(y,0) = 0 \tag{4}$$
$$V_x(y,b) = 0 \tag{5}$$
$$\tag{6}$$

It is important to highlight that particles will follow the flow profile. As such, particle tracking provides a means to optically probe the fluid flow. However, with channel heights significantly

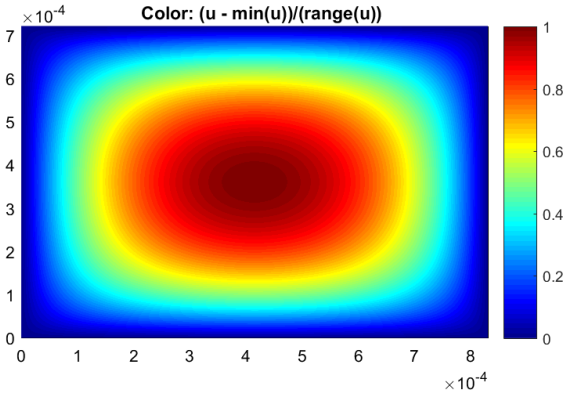


**FIGURE 5**: Normalized Flow Field in a 830.5 $\mu$m x 720 $\mu$m Rectangular Channel Cross Section

larger than the depth of focus of a microscope, optical probing is limited to a window of the flow. In order to quantify the flow, we employ a combination of theoretical and experimental techniques. Without fluorescence, we are limited to probing segments of the flow field. There exists a theoretical ratio between the maximum and average fluid velocity in a rectangular channel. As such, we focus the microscope such that the depth of focus contains the fastest moving particles in the microchannel. Using Green's functions to determine a series solution for the flow field described above, one obtains equation 7 where $P_{2n+1}$ and $Q_{2m+1}$ are defined by equations 8 and 9 respectively.

$$V_x(y,z) = \frac{\Delta p}{\mu L}\frac{16}{ab}\sum_{n,m=0}^{\infty}\frac{sin(P_{2n+1}y)sin(Q_{2m+1}z)}{P_{2n+1}Q_{2m+1}\left(P_{2n+1}^2+Q_{2m+1}^2\right)} \tag{7}$$

$$P_{2n+1} = \frac{\pi(2n+1)}{a} \tag{8}$$

$$Q_{2m+1} = \frac{\pi(2m+1)}{b} \tag{9}$$

Equation 10 illustrates the relationship between the maximum fluid velocity and the average fluid velocity. This relationship is utilized to estimate the average velocity in our microchannels. Equation 10 includes infinite sums as defined in equations 11 and 12 estimated by taking 10,000 terms. Each infinite sum was found to numerically converge exponentially fast.

$$V_{max}(a,b) = \frac{3}{2}\langle v \rangle \frac{1 - \frac{32}{\pi^3}S_4(a,b)}{1 - \frac{192}{\pi^5}S_3(a,b)} \tag{10}$$

$$S_3(a,b) = \sum_{m=0}^{\infty} \frac{1}{(2m+1)^5} tanh \frac{\pi a(2m+1)}{2b} \tag{11}$$

$$S_4(a,b) = \sum_{m=0}^{\infty} \frac{(-1)^m}{(2m+1)^3 cosh \frac{\pi a(2m+1)}{2b}} \tag{12}$$

Figure 6 illustrates the relationship between the ratio of maximum to average velocity and the channel aspect ratio. The aspect ratio (a/b) is defined as the ratio of channel width to channel height. For our 830.5 x 720 $\mu$m channels, the theoretical ratio was found to be 2.0916. Thus, by recording videos with the fastest moving particles in the depth of focus of the microscope, the average velocity of the microchannel flow can be determined without fluorescence – assuming a uniform particle distribution in the channel.

### 4.2 Mixing Metric

Figure 8 illustrates the mixing metric dependency on the number of resistor pulses per unit fluid passing over the resistor. Since the active micro-mixer is inherently pulsatory, we define our mixing metric to be a function of the number of pulses (or drive bubbles) each unit of fluid of length $L_r$ sees as it flows over the resistor. A residency time ($\tau_r$) is defined to illustrate

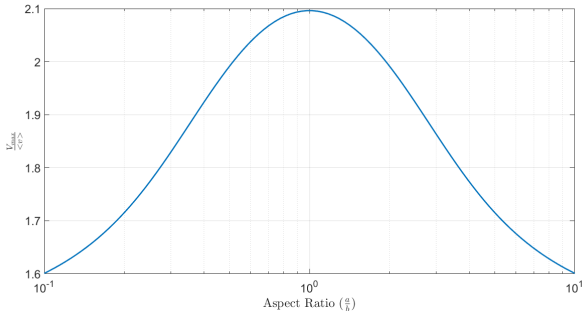


**FIGURE 6**: Relationship Between Ratio of Maximum to Average Velocity and Channel Aspect Ratio (a/b)

the amount of time it takes for fluid to pass over the resistor (see equation 13). $N_e$ describes the number of firing events that occurs within this fluid residency time (see equation 14). As such, the number of firing events that occurs can be controlled by two methods: (a) flow rates and (b) electrical firing frequency. Pulsing resistors at high frequencies risks electrical breakdown due to high current densities; as such, it is desirable to operate resistors under 500 Hz. By varying the flow rates, $N_e$ can be readily adjusted such that the resistor operates within electrical constraints.

$$\tau_r = \frac{L_r}{v_f} = \frac{L_R}{Q/A_c} = \frac{L_R A_c}{Q} \quad [s] \tag{13}$$

$$N_e = f\tau_r \tag{14}$$

$A_c$ [$m^2$] – cross-sectional area
$\tau_r$ [s] – residency time
$v_f$ [$\frac{m}{s}$] – fluid velocity
$Q$ [$\frac{m^3}{s}$] – flow rate
$f$ [Hz] – electrical resistor firing frequency
$N_e$ – number of pump events per unit fluid element over the resistor

In order to quantify mixing using particles, the output Y-leg of the channel was visualized. One input leg contained 7 $\mu m$ particles seeded in DI water while the other input leg contained DI water. To quantify the extent of mixing, a total particle count was performed in each leg of the output via custom MATLAB image processing scripts. The ratio of total particles counted in the lower leg (particle laden flow) and upper leg (DI water flow) was utilized to quantify mixing as illustrated in equation 15. From this metric, an ideal mixing scenario would consist initially of all

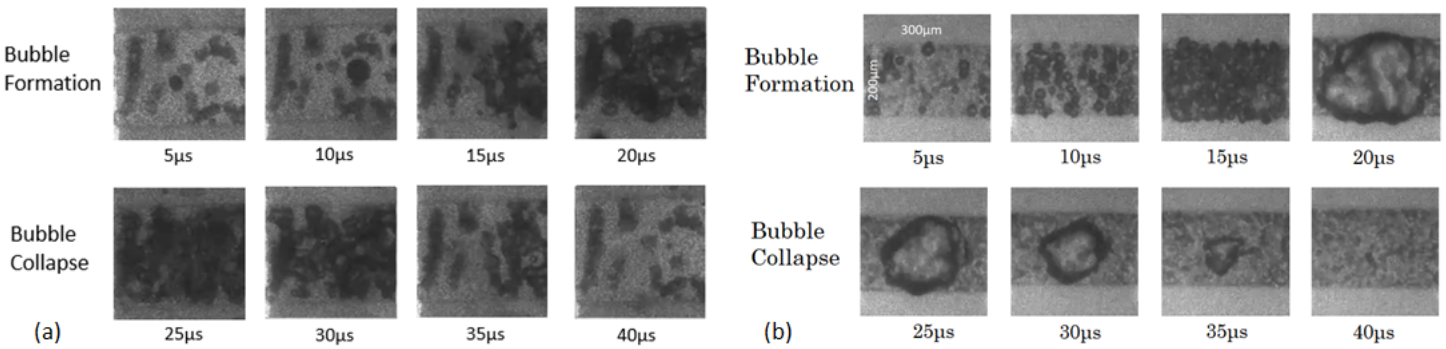


**FIGURE 7**: Bubble Dynamics – (a) nucleate boiling at 50 V, 10 $\mu$s pulse and (b) metastable boiling at 65 V, 10 $\mu$s pulse.

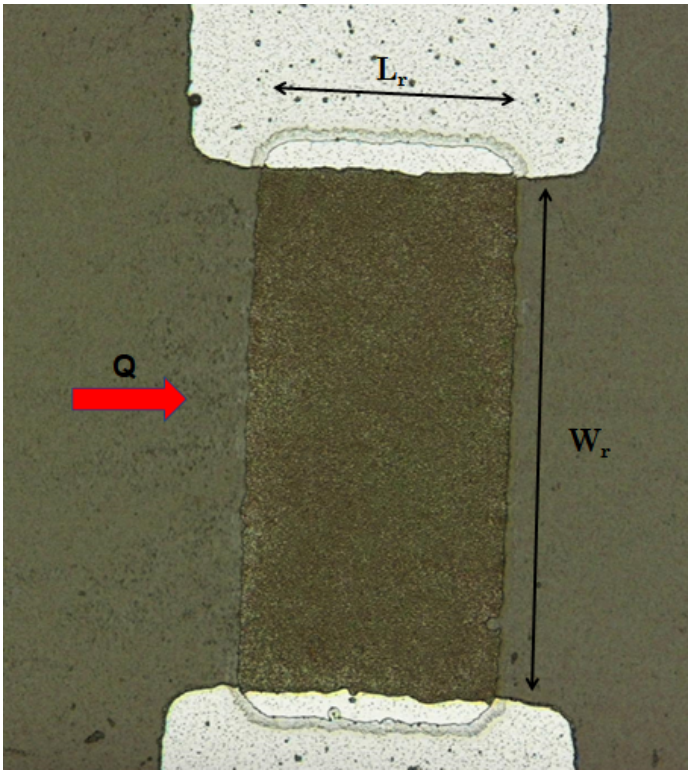


**FIGURE 8**: Resistor Dimensions – $L_r$ = 171.875 $\mu$m, $W_r$ = 325.875 $\mu$m, and film thickness = 0.71 $\mu$m.

particles in the lower leg and no particles in the upper leg, and, after perfect mixing, an equal amount of particles in the upper and lower legs. Thus, $M_{mixing}$ would go from 0 to 1.

$$M_{mixing} = \frac{total\ count\ upper\ leg}{total\ count\ lower\ leg} \tag{15}$$

## 5 Results

### 5.1 Bubble Nucleation and Boiling Modes

The surface temperature of the resistor can be used to control the boiling mode of the resistor. In this study, we look at the mixing efficiency for both nucleate and metastable boiling regimes. By adjusting the peak voltage pulse delivered to the resistor, the boiling mode could be toggled between nucleate and metastable boiling. Figure 7a demonstrates nucleate boiling using a 50 V, 10 $\mu s$ pulse. The bubble begins to nucleate approximately 5 $\mu s$ after the delivery of the voltage pulse. The bubble never fully expands and remains in nucleate boiling. A key consideration here is the surface roughness of the deposited polysilicon film. Through confocal microscope measurements of the resistor described in figure 8, the resistor's surface is characterized by a $R_a$ of 0.278 $\mu m$ (where $R_a$ denotes the arithmatic mean deviation of the surface). Enhanced surface roughness favors nucleation events on the resistor's surface which is unfavorable to achieve metastable boiling. However, by increasing the voltage and thus the surface temperature of the resistor, metastable boiling can be achieved. Figure 7b demonstrates metastable boiling using a 65 V, 10 $\mu s$ pulse. The bubble first begins to nucleate approximately 5 $\mu s$ after the delivery of the voltage pulse. By 20 $\mu s$, the bubble reaches its max expansion before collapsing at approximately 40 $\mu s$. This explosive expansion and collapse is theorized to cause mixing of laminar flows. As evidenced through the drive bubble formation, the surface roughness of the polysilicon film promotes an initial period of nucleate boiling before film boiling becomes evident. To eliminate this initial period of nucleate boiling, the surface roughness of the resistor should be reduced.

### 5.2 Macroscopic Mixing. One Pump. Firing Frequency

Primarily, we look at the nucleate boiling regime. Figure 9 illustrates particle streamlines representing the video averaged flow of particles through the microchannel. Without the resistor firing, figure 9a depicts particles entering the lower leg and exiting the lower leg – small streamlines in the upper leg are errors in

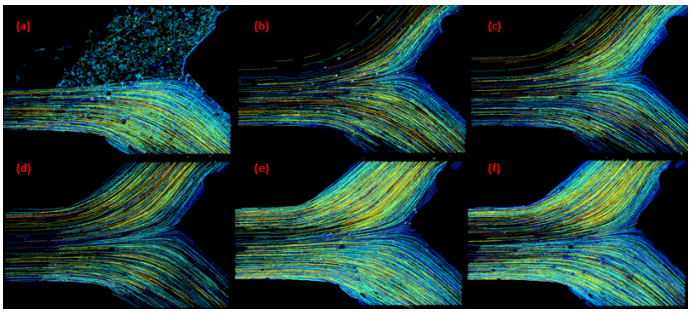


**FIGURE 9**: Nucleate Boiling Frequency Streamlines – displays particle streamlines across the entire video for various firing frequencies. (a) 0 Hz, (b) 5 Hz, (c) 10 Hz, (d) 15 Hz, (e) 20 Hz, and (f) 25 Hz.

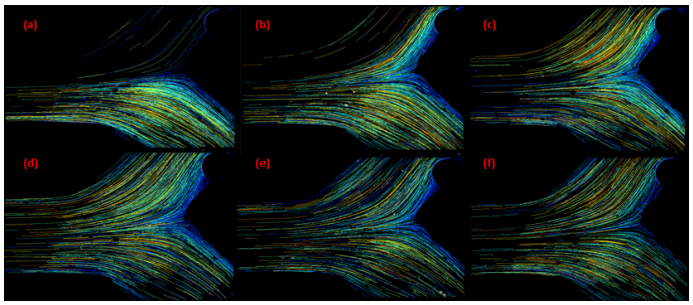


**FIGURE 10**: Metastable Boiling Frequency Streamlines – displays particle streamlines across the entire video for various firing frequencies. (a) 0 Hz, (b) 5 Hz, (c) 10 Hz, (d) 15 Hz, (e) 20 Hz, and (f) 25 Hz.

particle tracking and do not represent actual particle movement. As the resistor firing frequency increases, the extent of particle mixing also increases up to approximately 15 Hz in figure 9d upon which the particle-water mixture becomes homogenized. Figures 9b-c suggest that this mixing process is geometrically asymmetric at low frequencies. That is, the pulsatory mixing causes particles to first cross the laminar boundary closest to the original particle laden flow (at 5 Hz) and then begins to homogenize throughout the channel as the firing frequency increases.

Similarly, we look at the metastable boiling regime. Figure 10 illustrates particle streamlines under the metastable regime. Without resistor firing, figure 10a depicts particles entering the lower leg and exiting the lower leg. As the resistor firing frequency increases, particles become homogenized throughout the microchannel. Similar to the nucleate case, the mixing effect was observed to be geometrically asymmetric at low firing frequencies. A key observation in this study was that an overall mixing effect was observed in both nucleate and metastable boiling modes. As such, a single bubble is unnecessary to cause mixing; instead, bubbles nucleating in cavities on the resistor's surface provide sufficient fluid agitation to mix the fluids.

Applying the mixing metric defined by equation 15, figures 11 and 12 depict the relationship between the number of bubble events per unit fluid and the mixing effectiveness. As the number of bubble events ($N_e$) increases, the mixing effect increases towards an upper horizontal asymptote at which a mixing effect is not seen at higher $N_e$. Thus, there exists a critical number of of bubble events per unit fluid at which the resistor reaches its full mixing effectiveness. For the nucleate boiling regime, this critical point occurs at approximately 20 $N_e$ whereas, for metastable boiling, this critical point is at approximately 15 $N_e$. As such, both nucleate and metastable boiling modes were seen to significantly enhance the mixing of laminar flow with a mixing length of 171 $\mu m$.

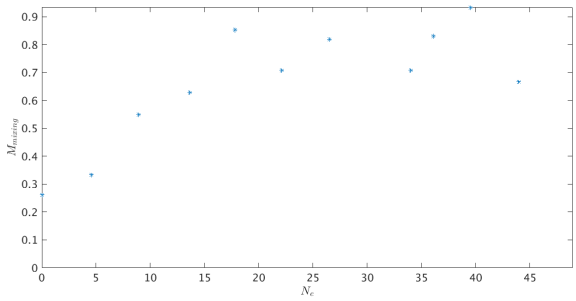


**FIGURE 11**: Nucleate Frequency Experiment

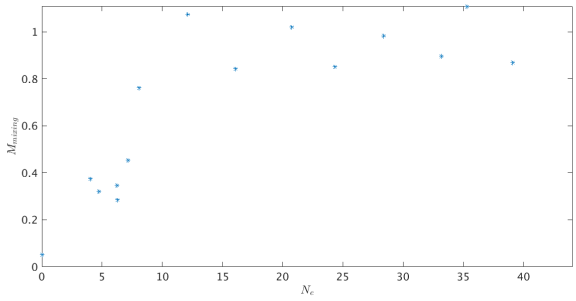


**FIGURE 12**: Metastable Frequency Experiment

## 6 Summary and Prospects

We conclude by asserting the extension of thermal inkjet technology to microfluidic mixing. Govyadinov, Kornilovitch, Markel, and Torniainen initially showed the extension of thermal inkjet technology as an integrated microfluidic pump [10] as well as theorized and simulated the extension of thermal inkjet technology as a micro-mixer [7]. We experimentally demonstrated the ability of thermal inkjet technology to mix laminar flow. In addition, we show that a net mixing effect can be seen in both

nucleate and metastable boiling regimes. A higher input voltage is required to reach metastable boiling than nucleate boiling. As such, the energy associated with microfluidic mixing could be substantially reduced by utilizing rough TIJ resistors operating in a nucleate boiling regime.

As lab-on-a-chip technologies continue to grow, the need for an integrated microfluidics platform becomes apparent. Thermal inkjet technology provides a way to integrate both unit microfluidic operations (such as sorting, mixing, dilution, ect.) as well as provides a way to integrate microfluidic pumps in such a system. The ability to integrate microfluidic pumps within microchannels makes thermal inkjet technology a strong contender for such a universal microfluidic platform.

## 7 Acknowledgements

The authors would like to thank Hewlett-Packard for sponsorship of this project; Katrina Sloma, Pavel Kornilovitch, Alex Govyadinov, Erik Torniainen, and David Markel for general and technical support of this project; Robert Pearson, Dale Ewbank, and Lynn Fuller for microfabrication insights and support; Michael Schrlau, Satish Kandlikar, and Steven Day for lab and equipment usage; and Patricia Clark, Sean O'Brien, and RIT SMFL staff for assistance with microfabrication processing.

## REFERENCES

[1] E.K. Sackmann, A.L. Fulton, D. B., 2011. "The present and future role of microfluidics in biomedical research". *Nature*.

[2] Streets Aaron M., Y. H., 2013. "Chip in a lab: Microfluidics for next generation life science research". *Biomicrofluidics*.

[3] Lee C-Y, Chang C-L, W. Y.-N. F. L.-M., 2011. "Microfluidic mixing: A review". *International Journal of Molecular Sciences*.

[4] A. Stroock, S. Dertinger, A. Ajdari, I. Mezić, H. Stone, and G. Whitesides, 2002. "Chaotic mixer for microchannels". *Science,* ***295***, pp. 647–651.

[5] Y. Liu and B. Kim and H. Sung, 2004. "Two-fluid mixing in a microchannel". *International Journal of Heat and Fluid Flow,* ***25***, July, pp. 986–995.

[6] D. Owen, M. Ballard, A. Alexeev, and P. Hesketh, 2016. "Rapid microfluidic mixing via rotating magnetic microbeads". *Sensors and Actuators A: Physical,* ***251***, September, pp. 84–94.

[7] A.N. Govyadinov, E.D. Torniainen, P. K. D. M., 2015. "Path to low cost microfluidics". *NIP Digital Fabrication Conference*.

[8] J. Stasiak, S. Richards, P. B., 2012. "Hewlett-packard's mems technology: Thermal inkjet printing". *Microelectronics to Nanoelectronics: Materials, Devices Manufacturability*.

[9] B. Hayes, A.N. Govyadinov, P. K., 2015. "Microfluidic switchboards with integrated inertial pumps". *Microfluidics and Nanofluidics,* ***22***.

[10] A.N. Govyadinov, P.E. Kornilovitch, D. M. E. T., 2016. "Single-pulse dynamics and flow rates of inertial micropumps". *Microfluidics and Nanofluidics*.

[11] Crocker, J. C., and Grier, D. G., 1996. "Methods of digital video microscopy for colloidal studies". *Journal of Colloid and Interface Science,* ***179***(1), pp. 298 – 310.